Ultra-bright, Efficient and Stable Perovskite Light-Emitting Diodes

Joo Sung Kim[1,†], Jung-Min Heo[1,†], Gyeong-Su Park[1,2,3], Seung-Je Woo[1], Changsoon Cho[4],

Hyung Joong Yun[5], Dong-Hyeok Kim[1], Jinwoo Park[1], Seung-Chul Lee[6,7], Sang-Hwan Park[1],

Eojin Yoon[1], Neil C. Greenham[4], and Tae-Woo Lee[1,2,7,8,]*

[1]*Department of Materials Science and Engineering, Seoul National University, 1 Gwanak-ro Gwanak-gu, Seoul 08826, Republic of Korea*

[2] *Research Institute of Advanced Materials, Seoul National University, 1 Gwanak-ro, Gwanak-gu, Seoul 08826, Republic of Korea*

[3]*Institute of Next-Generation Semiconductor Convergence Technology, Daegu Gyeongbuk Institute of Science and Technology (DGIST), Daegu 42988, Republic of Korea*

[4]*Cavendish Laboratory, Department of Physics, University of Cambridge, J.J. Thomson Avenue, Cambridge, CB3 0HE, UK*

[5]*Advanced Nano Research Group, Korea Basic Science Institute (KBSI), Daejeon, 34133, Republic of Korea*

[6]*PEROLED Co. Ltd., Building 940, 1 Gwanak-ro, Gwanak-gu, Seoul, Republic of Korea*

[7]*Soft Foundry, Seoul National University, 1 Gwanak-ro, Gwanak-gu, Seoul 08826, Republic of Korea*

[8]*School of Chemical and Biological Engineering, Institute of Engineering Research, Seoul National University, 1 Gwanak-ro, Gwanak-gu, Seoul 08826, Republic of Korea.*

21   †*These Authors contributed equally to this work*

22   **Authors to whom correspondence should be addressed: E-mail: twlees@snu.ac.kr,*

23   *taewlees@gmail.com*

24   **Abstract**

25   Metal halide perovskites are attracting great attention as next-generation light emitting
26   materials due to their excellent emission properties with narrowband emission.[1–4] However,
27   perovskite light-emitting didoes (PeLEDs) irrespective of their material types (polycrystals or
28   nanocrystals) have not realized high luminance, high efficiency and long lifetime
29   simultaneously, as they are influenced by the intrinsic limitations related to the trade-off
30   properties between charge transport and confinement in each type of perovskite materials.[5–8]
31   Here, we report an ultra-bright, efficient, and stable PeLEDs made of core/shell perovskite
32   nanocrystals with a size of ~10 nm obtained using simple *in-situ* reaction of benzylphosphonic
33   acid (BPA) additive with 3D polycrystalline perovskite films without separate synthesis
34   process. During the reaction, large 3D crystals are split into nanocrystals and the BPA surrounds
35   the nanocrystals, achieving strong carrier confinement. The BPA shell passivates the
36   undercoordinated lead atoms by forming covalent bonds, and thereby greatly reduces trap
37   density while maintaining good charge-transport properties of 3D perovskites. We demonstrate
38   simultaneously efficient, bright, and stable PeLEDs that have maximum brightness of ~470,000
39   cd m^{-2}, maximum external quantum efficiency of 28.9 % (average = 25.2 ± 1.6 % over 40
40   devices), maximum current efficiency of 151 cd A^{-1}, and half-lifetime of 520 h at 1,000 cd m^{-2}
41   (estimated half-lifetime >30,000 h at 100 cd m^{-2}). Our work sheds great light on the possibility
42   that PeLEDs can be commercialized in the future display industry.

43

Introduction

Metal halide perovskites (MHPs) are being studied as promising candidates for light emitters due to their narrow emission spectra (full-width at half maximum (FWHM) ≈ 20 nm), easy color tuning, excellent charge transport properties, and low-cost solution processability[1–4]. Because of these advantages, research has mainly focused on achieving highly-efficient operation of perovskite light-emitting diodes (PeLEDs). By introducing a perovskite nanocrystal structure synthesized with organic ligands or cation alloying (e.g. FAGAPbBr$_3$), high current efficiency of 108 cd A^{-1} and external quantum efficiency (EQE) of 23.4 % were achieved by realizing strong carrier confinement and bulk/surface defect suppression[3,5–12]. However, in these perovskite nanocrystal emitters, the insulating characteristics of organic ligands can impede charge injection and transport, and thereby limit the brightness at the given voltage and the operational lifetime despite their high luminous efficiency[8,13–15]. In contrast, 3D polycrystalline perovskite (hereafter, 3D perovskite) film without such organic ligands has good charge transport characteristics and simple fabrication processes (maximum luminance >100,000 cd m^{-2}, device half-lifetime (T_{50}) > 200 h at initial brightness = 100 cd m^{-2}), but suffers from low luminous efficiency because of the poor charge confinement effect in the big grains of >100 nm and non-radiative recombination defects at the grain boundary[16–20]. Although the improvements in both perovskite nanocrystals and 3D perovskites have enabled drastic advances in the EQE of PeLEDs, due to the inevitable trade-off between these charge confinement and charge transport, the state-of-the-art efficient PeLEDs with maximum EQE >20 % mostly suffer from low brightness (~10,000 cd m^{-2})[7,10,15] and short T_{50} (< 100 h at initial brightness = 100 cd m^{-2})[10]. Therefore, developing a perovskite material system that allow high brightness, high efficiency and long device lifetime simultaneously is of great importance at the current stage of research on PeLEDs.

Here, we developed a simple method to produce *in-situ* formed core/shell nanoparticles (hereafter, *in-situ* core/shell) by reacting 3D perovskite films with benzylphosphonic acid (BPA), which can split large crystals into perovskite nanoparticles (PeNPs) and surround them to form PeNP@BPA composite, in which BPA exist as an organic shell material[21]. Significantly reduced particle size of *in-situ* core/shell nanocrystals (10 ± 2 nm) compared with that of the 3D perovskites (205 ± 97 nm) showed significantly improved carrier confinement, and the phosphonate group of BPA effectively passivated the defect sites

75   by binding covalently to undercoordinated Pb^{2+}. In the *in-situ* core/shell perovskite NPs, the

76   trap density was greatly decreased and the radiative recombination efficiency was significantly

77   increased compared to the 3D perovskites. PeLEDs based on *in-situ* core/shell structure showed

78   maximum current efficiency of 151 cd A^{-1} (maximum EQE of 28.9 %), maximum brightness

79   of ~470,000 cd m^{-2}, very little efficiency roll-off (~5 % even at 400,000 cd m^{-2}) and half-

80   lifetime of 520 h at initial brightness of 1,000 cd m^{-2} (estimated half-lifetime >30,000 h at 100

81   cd m^{-2}) with green emission at EL peak of 540 nm, and therefore shows excellent efficiency,

82   luminance, and lifetime simultaneously.

83   **Results**

84   ***In-situ* nanostructure formation by BPA treatment**

85   We first show how post-treatment using BPA forms the *in-situ* nanostructure of the

86   perovskite crystal. 3D perovskite film of $(FA_{0.7}MA_{0.1}GA_{0.2})_{0.87}Cs_{0.13}PbBr_3$ was fabricated (left

87   of **Fig. 1a**) using the additive-based nanocrystal pinning (A-NCP) method[3]. In this case, ionic

88   defects with low formation energy exist on the crystal surface and inside the crystal, acting as

89   a cause of ion migration and carrier trapping, thereby significantly reducing the luminescence

90   efficiency and operational stability[19]. First, we added BPA as an additive into the precursor

91   solution, implementing an *in-situ* particle structure in which BPA cover the surface of crystals

92   by attaching as a ligand to the undercoordinated Pb on the surface of 3D perovskites (center of

93   **Fig. 1a**). The surface of the 3D perovskite film initially had an amorphous and irregular shape

94   due to a defective surface; after addition of up to 10 mol. % of BPA into the precursor, the

95   fabricated film developed a very clear cubic structure as the BPA molecules assembled on the

96   surface (**Extended Data Fig. 1**).

97   The perovskite thin film was further exposed to a BPA solution in tetrahydrofuran

98   (THF), forming *in-situ* core/shell perovskite NPs (right of **Fig. 1a**). Unlike other long alkyl

99   ligands (e.g. oleic acid, decylamine, and octylphosphonate), small BPA molecules with strong

100   acidity can penetrate and intercalate into large perovskite crystals[22]. After sufficient time is

101   provided for the BPA to intercalate into the crystal, BPA binds to the surface sites within the

102   crystal and splits the large crystal domain into a nanosized *in-situ* core/shell structure that is

103   surrounded by BPA.

The progressive particle refinement of large 3D perovskite grain to *in-situ* core/shell perovskite NPs was observed by high-resolution transmission electron microscopy (TEM). With increasing reaction time in BPA-THF solution, initially rectangular 3D crystals with size of 200 nm showed gradual change in grain shape and decrease of grain size, and finally became spherical *in-situ* core/shell structured nanograins with a size of 10 nm. (**Fig. 1b-i**) The *in-situ* core/shell synthesis process was further confirmed using atomic-scale scanning transmission electron microscopy (STEM) and scanning electron microscopy (SEM). At the beginning of the reaction, BPA molecules bind to defective surfaces of large crystals that appear as dark contrast regions or vague boundaries on STEM images, cracking the crystal out and thus reducing the grain size (**Extended Data Fig. 2a-c**). The grain splitting reveals new defective surfaces, and the cycle of BPA binding and breakage repeats and the grain size gradually decreased with increased coverage of a BPA shell on the surface (**Extended Data Fig. 2d-g**). Finally, when BPA molecules fully surround the 3D core that lacks a defective surface to which BPA can bind, the *in-situ* core/shell structure is achieved (**Fig. 1e,i**). Perfect 3D lattice structure in the core part and clear core/shell interface between perovskite and BPA molecule was identified by STEM image and electron energy loss spectra (EELS) (**Fig. 1j-l, Extended Data Fig. 3**). When the *in-situ* core/shell synthesis is finished, these *in-situ* core/shell grains are located adjacent to each other, after being aggregated by the excess BPA molecules around them to form macroparticles, as observed in SEM and TEM images and EDS maps (**Extended Data Fig. 4-5**). The grain size distribution of these perovskite grains significantly decreased from the 3D perovskite (205 ± 97 nm) to the *in-situ* particle structure (123 ± 34 nm) and further to the *in-situ* core/shell structure (10 ± 2 nm) (**Supplementary Data Fig. 1**).

Surface passivation of BPA shell

To elucidate the mode of binding between BPA and the perovskite structure, we performed X-ray photoelectron spectroscopy (XPS) and ultraviolet photoelectron spectroscopy (UPS) analysis. The existence of BPA in perovskite films can be confirmed by emergence of new peak at P 2p and O 1s spectra only in *in-situ* particle and *in-situ* core/shell perovskites (**Supplementary Fig. 2a-b**). The O 1s spectrum of the BPA prior to any reaction shows the main oxygen peak from the P-OH group at 533.0 eV and the P=O group at 531.5 eV in a ratio

134   of 2:1, which is consistent with previously-reported O 1s spectra of phosphonic acid derivatives

135   (**Fig. 2a**)[23,24]. In contrast, in the O 1s peak of *in-situ* particles and *in-situ* core/shell perovskites,

136   a new peak around 531.0 eV appeared (**Fig. 2b-c**). This change can be ascribed to the formation

137   of covalent bonds during adsorption of phosphonate onto a metallic surface[23,25]. i.e., BPA bonds

138   to the surface of perovskites by forming a new Pb-O-P covalent bond and replaces the bromide

139   vacancy site. In addition, the Pb 4f peak and the Br 3d peak of the BPA-induced structures are

140   shifted to higher binding energy than in the 3D perovskite structure. This difference can be

141   attributed to higher electronegativity of oxygen atoms compared with that of bromines, and

142   therefore modifying the Fermi level (**Supplementary Fig. 2c-d**). This can also be confirmed

143   by UPS analysis, which showed that the *in-situ* particle and *in-situ* core/shell particle have

144   much lower work function and higher energy offset between the work function and valence

145   band (**Supplementary Fig. 3**, **Fig. 2d**). This difference can arise from gradual diminishing of

146   self p-doping effects caused by ionic defects at the surface and within the crystal in 3D

147   perovskite and *in-situ* particle perovskite, which was suppressed in the *in-situ* core/shell

148   particle.

149

150   **Improvement in emission characteristics and defect passivation**

151   We analyzed the luminescence properties by conducting photoluminescence quantum

152   efficiency (PLQE) analysis. While perovskite thin films based on 3D and *in-situ* particle

153   structure showed comparably low internal quantum efficiency (IQE) of 30 % and 35 %

154   respectively, *in-situ* core/shell perovskite film showed greatly high IQE of 88 % (**Extended**

155   **Data Fig. 6a-c**). Steady-state PL spectra and time-correlated single photon counting (TCSPC)

156   measurement also confirmed higher PL intensity and longer PL lifetime in *in-situ* core/shell

157   structure compared to that in 3D and *in-situ* particle perovskites (**Fig. 3a-b**). The great

158   improvement of IQE can be realized by reducing the particle size to strengthen charge

159   confinement and defect density by passivating defects, i.e., undercoordinated Pb atoms and

160   halide vacancies, which act as non-radiative recombination centers in the perovskite emitter.

161   The improved charge confinement was confirmed by temperature-dependent PL analysis (**Fig.**

162   **3c-e, Extended Data Fig. 6d-i**). From 3D to *in-situ* particle and *in-situ* core/shell structure, the

163   peak center was blue-shifted, and the exciton binding energy (E_b) was increased from 90 meV

164   to 220 meV; this change indicates that the *in-situ* core/shell structure experiences a strong
165   confinement effect from the grain size reduction.

166   To further confirm the passivation effect of BPA-induced nanostructure, we performed
167   trap-density analysis by fabricating hole-only device (HOD) and analyzing the transport
168   characteristics (**Supplementary Fig. 4**). The current-voltage (I-V) characteristics of these
169   HOD can be classified into three types of region according to the slope (k), Ohmic region ($k =$
170   1) in the low-injection regime, a trap-filled limited (TFL) region ($k > 3$), and a space-charge
171   limited current (SCLC) regime ($k = 2$)[26]. In this, the total trap state density inside the perovskite
172   film can be calculated as

173    $$n_t = 2\varepsilon\varepsilon_0 V_{TFL}/(eL^2)$$

174   where n_t is the trap state density, V_{TFL} is the trap-filled limit voltage, L is the thickness of the
175   perovskites, e is the elementary charge, ε_0 and ε are the vacuum permittivity and relative
176   permittivity, respectively. By estimating V_{TFL} as the intersection between ohmic region and
177   TFL region, we calculate $n_t = 3.50 \times 10^{16}$ cm^{-3} for 3D, $n_t = 2.36 \times 10^{16}$ cm^{-3} for *in-situ* particle, n_t
178    $= 1.37 \times 10^{16}$ cm^{-3} for *in-situ* core/shell perovskites. This result is evidence that the passivation
179   effect of BPA-induced nanostructure in perovskite films also contributes to the increased
180   luminescent efficiency. We also calculated the hole mobility (μ_h) of each device by applying
181   the Mott–Gurney law equation in the Child region of trap-free SCLC transport as below.

182    $$\mu_h = \frac{8L^3 J}{9\varepsilon\varepsilon_0 V^2}$$

183   Here, J is the current density, and V is the voltage. All devices had similar μ_h: 3.26×10^{-2} cm^2
184   V^{-1} s^{-1} with 3D, 3.08×10^{-2} cm^2 V^{-1} s^{-1} with *in-situ* particle, and 2.99×10^{-2} cm^2 V^{-1} s^{-1} with *in-*
185   *situ* core/shell perovskites. This result indicates that fast charge transport property in 3D
186   perovskites could be preserved in the *in-situ* core/shell structure because excessive insulating
187   ligand was not used.

188   **Light-emitting diode performance**

189   Encouraged by simultaneously increased PL efficiency, decreased trap density, and
190   preserved fast charge transport, we fabricated LEDs based on the BPA-induced nanostructured
191   perovskites (**Fig. 4a, Supplementary Fig. 5**). The PeLEDs based on *in-situ* core/shell

192 perovskites showed maximum current efficiency of 151 cd A^{-1} and maximum EQE of 28.9 %,

193 calculated using the full angular electroluminescence distribution (**Fig. 4b-c, Extended Data**

194 **Fig. 7a-g**)[27]. In contrast to many previously-reported OLEDs and PeLEDs that have ultrathin

195 EMLs (< 50 nm), this is a remarkably high EQE with an EML > 200 nm in devices in which

196 the microcavity effects are diluted. The result emphasizes the important role of photon

197 recycling effect in thick EMLs[28–31]. Optical simulation verified that our PeLEDs can reach EQE

198 of 29.2 % with an aid of photon recycling effect (**Supplementary Fig. 6**). The detailed current-

199 voltage-luminance characteristics are summarized in **Extended Data Table 1**. Also, the

200 distribution of EQE and luminance obtained from 40 devices showed great reproducibility (**Fig.**

201 **4d, Extended Data Fig. 7h**). Especially, to manufacture efficient *in-situ* core/shell PeLEDs

202 with great reproducibility, the crystallization process of as-synthesized perovskite thin films

203 must be controlled so that the grain size does not increase too much before the *in-situ* reaction

204 with BPA. When the A-NCP timing is not delayed and the processing temperature is kept <

205 18 °C, the grain size can be sufficiently small (< 100 nm), so that BPA can completely penetrate

206 them during the reaction, and thereby provide nanostructures that are favorable for obtaining

207 high-efficiency devices (**Extended Data Fig. 7i**). The PeLEDs showed high maximum

208 brightness of 473,990 cd m^{-2} whereas 3D PeLEDs and *in-situ* particle PeLEDs showed

209 maximum brightness of only 20,271 cd m^{-2} and 149,331 cd m^{-2}, respectively. The maximum

210 brightness of *in-situ* core/shell PeLEDs is the highest so far reported among PeLEDs based on

211 any of the 3D, quasi-2D, or perovskite nanocrystals, and is even comparable with the highest

212 brightness of state-of-the-art inorganic quantum dot (QD) LEDs (**Fig. 4e**)[32]. Furthermore, due

213 to the fast charge transport with high IQE, we could realize ultralow driving voltage of 2.7 V

214 at brightness of 10,000 cd m^{-2}, which is much lower than the driving voltage of any other state-

215 of-the-art LEDs based on Quasi-2D (4.7 V), PeNC (~6 V), or organic Ir(ppy)$_2$(acac) (~4.8 V)

216 (**Supplementary Table 1**). *In-situ* core/shell PeLEDs also maintained the EQE value of ≥20 %

217 under ultra-high brightness conditions from 50,000 cd m^{-2} to 400,000 cd m^{-2}, and exhibited

218 very low roll-off of ~ 5 % at luminance of 400,000 cd m^{-2} (**Supplementary Table 2**). These

219 results are remarkable considering that reported high-efficiency nanocrystal PeLEDs with EQE

220 > 20 % have low brightness (~10,000 cd m^{-2}) and large efficiency roll-off (>50 % at >10,000

221 cd m^{-2}), because they use insulating ligands and therefore have thickness of emitting layer

222 mostly < 30 nm to compensate its poor charge-transporting characteristics and to strengthen

223   light outcoupling from the device (**Fig. 4e**). In contrast, *in-situ* core/shell perovskites are

224   formed by *in-situ* treatment of 3D perovskites without long insulating ligands, so both high

225   efficiency and high brightness could be realized without significantly sacrificing charge

226   transport, which in turn resulted in low-efficiency roll-off because of better charge balance with

227   higher charge transport and thus no severe charge accumulation. We also fabricated bright

228   large-area PeLEDs (pixel size: 120 mm^2) based on *in-situ* core/shell structure. These PeLEDs

229   had high uniformity and efficiency >20 %; these results show the potential of hybrid perovskite

230   emitters for use in solid-state lighting and display applications (**Fig. 4f, Extended Data Fig.**

231   **8**).

232   Finally, the operational lifetime of the PeLEDs were analyzed by applying a constant

233   current and monitoring the luminance. Compared with the T_{50} of 3D (0.2 h) and *in-situ* particle

234   (3.5 h) PeLEDs at initial brightness (L_0) = 10,000 cd m^{-2}, *in-situ* core/shell PeLEDs showed

235   much longer T_{50} of 14 h, due to greatly improved luminescent efficiency without sacrifice of

236   charge-transport properties (**Extended Data Fig. 9**). The operational lifetime of *in-situ*

237   core/shell PeLEDs was further measured at various L_0 from 1,000 cd m^{-2} to 200,000 cd m^{-2}

238   (**Fig. 4g-h**). Specifically, *in-situ* core/shell PeLEDs showed ultra-long T_{50} of 520 h at 1,000 cd

239   m^{-2}. By using the accelerated lifetime equation ($L_0^n T_{50}$ = constant, where *n* is an acceleration

240   factor)[33,34] with *n* = 1.68 over 21 devices, we estimated the device's T_{50} at 100 cd m^{-2} to be

241   31,808 h, which is, to our knowledge, the highest T_{50} estimated to date in PeLEDs (**Fig. 4h-i,**

242   **Supplementary Table 3**).

243   **Conclusions**

244   We demonstrated *in-situ* core/shell perovskite nanocrystals with size of ~10 nm by

245   using *in-situ* reaction of BPA molecule with 3D perovskite thin films. In the process of reaction,

246   BPA molecules penetrated into large 3D perovskite crystals and split them into nanosized

247   crystals, thus surrounding it as a core/shell structure. This *in-situ* core/shell NP structure

248   enabled increased carrier confinement, reduction in trap density, and increase in luminous

249   efficiency without sacrificing the charge transport properties of 3D perovskites. As a result,

250   simultaneously ultra-bright, efficient and stable PeLEDs with maximum current efficiency of

251   151 cd A^{-1} (maximum EQE of 28.9 %), maximum luminance of ~470,000 cd m^{-2}, very low

252   efficiency roll-off of ~5 % at 400,000 cd m^{-2}, and half-lifetime of 520 h at initial brightness of

253 1,000 cd m^{-2} (estimated half-lifetime >30,000 h at 100 cd m^{-2}) were demonstrated. These results

254 suggest that PeLEDs are not only laboratory-level high-efficiency devices but are promising

255 candidates for commercial self-emissive displays and lighting applications that require ultra-

256 high brightness and long operational lifetime comparable to those of state-of-the-art OLEDs or

257 QD LEDs.

258

Reference

1. Kim, Y.-H. *et al.* Multicolored Organic/Inorganic Hybrid Perovskite Light-Emitting Diodes. *Adv. Mater.* **27**, 1248–1254 (2015).

2. Tan, Z.-K. *et al.* Bright light-emitting diodes based on organometal halide perovskite. *Nat. Nanotechnol.* **9**, 687–692 (2014).

3. Cho, H. *et al.* Overcoming the electroluminescence efficiency limitations of perovskite light-emitting diodes. *Science (80-.).* **350**, 1222–1225 (2015).

4. Kim, Y.-H., Cho, H. & Lee, T.-W. Metal halide perovskite light emitters. *Proc. Natl. Acad. Sci. U. S. A.* **113**, 11694–11702 (2016).

5. Yang, X. *et al.* Efficient green light-emitting diodes based on quasi-two-dimensional composition and phase engineered perovskite with surface passivation. *Nat. Commun.* **9**, 2–9 (2018).

6. Zhao, B. *et al.* High-efficiency perovskite–polymer bulk heterostructure light-emitting diodes. *Nat. Photonics* **12**, 783–789 (2018).

7. Kim, Y.-H. *et al.* Comprehensive defect suppression in perovskite nanocrystals for high-efficiency light-emitting diodes. *Nat. Photonics* **15**, 148–155 (2021).

8. Hassan, Y. *et al.* Ligand-engineered bandgap stability in mixed-halide perovskite LEDs. *Nature* **591**, 72–77 (2021).

9. Xiao, Z. *et al.* Efficient perovskite light-emitting diodes featuring nanometre-sized crystallites. *Nat. Photonics* **11**, 108–115 (2017).

10. Lin, K. *et al.* Perovskite light-emitting diodes with external quantum efficiency exceeding 20 per cent. *Nature* **562**, 245–248 (2018).

11. Kim, Y.-H., Kim, J. S. & Lee, T. Strategies to Improve Luminescence Efficiency of Metal-Halide Perovskites and Light-Emitting Diodes. *Adv. Mater.* **31**, 1804595 (2019).

12. Park, M.-H. *et al.* Boosting Efficiency in Polycrystalline Metal Halide Perovskite Light-Emitting Diodes. *ACS Energy Lett.* **4**, 1134–1149 (2019).

13. Cho, H., Kim, Y.-H., Wolf, C., Lee, H.-D. & Lee, T.-W. Improving the Stability of Metal Halide Perovskite Materials and Light-Emitting Diodes. *Adv. Mater.* **30**, 1704587 (2018).

14. Liu, M., Matuhina, A., Zhang, H. & Vivo, P. Advances in the Stability of Halide Perovskite Nanocrystals. *Materials (Basel).* **12**, 3733 (2019).

15. Dong, Y. *et al.* Bipolar-shell resurfacing for blue LEDs based on strongly confined perovskite quantum dots. *Nat. Nanotechnol.* **15**, 668–674 (2020).

16. Wehrenfennig, C., Eperon, G. E., Johnston, M. B., Snaith, H. J. & Herz, L. M. High Charge Carrier Mobilities and Lifetimes in Organolead Trihalide Perovskites. *Adv. Mater.* **26**, 1584–1589 (2014).

17. Herz, L. M. Charge-Carrier Mobilities in Metal Halide Perovskites: Fundamental

296   Mechanisms and Limits. *ACS Energy Lett.* **2**, 1539–1548 (2017).

297   18.   Xu, W. *et al.* Rational molecular passivation for high-performance perovskite light-
298   emitting diodes. *Nat. Photonics* **13**, 418–424 (2019).

299   19.   Meggiolaro, D., Mosconi, E. & De Angelis, F. Formation of Surface Defects
300   Dominates Ion Migration in Lead-Halide Perovskites. *ACS Energy Lett.* **4**, 779–785
301   (2019).

302   20.   Zhang, L. *et al.* Suppressing Ion Migration Enables Stable Perovskite Light-Emitting
303   Diodes with All-Inorganic Strategy. *Adv. Funct. Mater.* **30**, 1–8 (2020).

304   21.   Ahmed, G. H., Yin, J., Bakr, O. M. & Mohammed, O. F. Successes and Challenges of
305   Core/Shell Lead Halide Perovskite Nanocrystals. *ACS Energy Lett.* **6**, 1340–1357
306   (2021).

307   22.   Park, S. M., Abtahi, A., Boehm, A. M. & Graham, K. R. Surface Ligands for
308   Methylammonium Lead Iodide Films: Surface Coverage, Energetics, and Photovoltaic
309   Performance. *ACS Energy Lett.* **5**, 799–806 (2020).

310   23.   Wagstaffe, M. *et al.* An Experimental Investigation of the Adsorption of a Phosphonic
311   Acid on the Anatase TiO 2 (101) Surface. *J. Phys. Chem. C* **120**, 1693–1700 (2016).

312   24.   Li, F., Zhong, H., Zhao, G., Wang, S. & Liu, G. Adsorption of α-hydroxyoctyl
313   phosphonic acid to ilmenite/water interface and its application in flotation. *Colloids*
314   *Surfaces A Physicochem. Eng. Asp.* **490**, 67–73 (2016).

315   25.   Xuan, T. *et al.* Highly stable CsPbBr 3 quantum dots coated with alkyl phosphate for
316   white light-emitting diodes. *Nanoscale* **9**, 15286–15290 (2017).

317   26.   Kim, H. *et al.* Proton-transfer-induced 3D/2D hybrid perovskites suppress ion
318   migration and reduce luminance overshoot. *Nat. Commun.* **11**, 3378 (2020).

319   27.   Jeong, S.-H. *et al.* Characterizing the Efficiency of Perovskite Solar Cells and Light-
320   Emitting Diodes. *Joule* **4**, 1206–1235 (2020).

321   28.   Pazos-Outon, L. M. *et al.* Photon recycling in lead iodide perovskite solar cells.
322   *Science (80-.).* **351**, 1430–1433 (2016).

323   29.   Stranks, S. D., Hoye, R. L. Z., Di, D., Friend, R. H. & Deschler, F. The Physics of
324   Light Emission in Halide Perovskite Devices. *Adv. Mater.* **31**, 1803336 (2019).

325   30.   Cho, C. *et al.* The role of photon recycling in perovskite light-emitting diodes. *Nat.*
326   *Commun.* **11**, 1–8 (2020).

327   31.   Cho, C. & Greenham, N. C. Computational Study of Dipole Radiation in Re-
328   Absorbing Perovskite Semiconductors for Optoelectronics. *Adv. Sci.* **8**, 2003559
329   (2021).

330   32.   Song, J. *et al.* Over 30% External Quantum Efficiency Light-Emitting Diodes by
331   Engineering Quantum Dot-Assisted Energy Level Match for Hole Transport Layer.
332   *Adv. Funct. Mater.* **29**, 1808377 (2019).

333   33.   Dai, X. *et al.* Solution-processed, high-performance light-emitting diodes based on

12

334   quantum dots. *Nature* **515**, 96–99 (2014).

335   34.   Woo, S.-J., Kim, J. S. & Lee, T.-W. Characterization of stability and challenges to
336   improve lifetime in perovskite LEDs. *Nat. Photonics* **15**, 630–634 (2021).

337

343

344   **Author Contributions** J.S.K., J.-M.H. equally contributed to this work. J.S.K., J.-M. H. and

345   T.-W.L. initiated and designed the study. J.S.K and J.-M.H. fabricated LED devices and

346   analyzed data. G.-S.P. performed the TEM measurement. H.J.Y. conducted the UPS and XPS

347   analysis. S.-J. W. and D.-H. Kim conducted the temperature-dependent PL and

348   photoluminescence quantum efficiency analysis. S.-J.W. and C.C conducted the optical

349   simulation of the devices. J.P. assisted to analyze the TCSPC data. S.-C.L. provided support

350   for the characterization of the materials. S.-H.P. and E.Y. assisted the fabrication of LED

351   devices. T.-W.L. supervised the work. J.S.K. drafted the first version of the manuscript, with

352   assistance from J.-M.H. and T.-W.L. All authors discussed the results and commented on the

353   manuscript.

354   **Competing interests** The authors declare no competing interests.

355

356

Fig. 1 | Emergence of *in-situ* core/shell perovskite with BPA treatment. a, Schematic illustration of the transformation process of 3D (left) into *in-situ* particle (middle) and *in-situ* core/shell (right) structure by BPA treatment. TEM image of perovskite nanograins during *in-situ* core/shell synthesis process with reaction time of **b**, 1 s, **c,** 10 s, **d,** 20 s, **e,** 30 s. (insets: low-magnification TEM images). **f-h,** High-resolution TEM images of the boxed regions in **b-d**. (insets: FFT-diffractograms showing the cubic lattice structure) **i,** High-resolution HAADF-STEM image of the single *in-situ* core/shell NP taken from the boxed region in **e,** showing a flat interface between the perovskite core and the BPA shell. **j,** Atomically resolved HAADF-STEM image of the core region taken from the *in-situ* core/shell perovskite NP with atomic structure model, showing the perfect 3D perovskite crystal structure. **k,** High-resolution STEM image focusing on surface region of *in-situ* core/shell. **l,** the EEL spectra acquired from the positions A and B highlighted in **k**. The Si peak is a background signal from the silicon nitride TEM window grid.

Fig. 2 | Surface passivation of BPA ligand. a-c, O 1s XPS core-level spectra of **a**, BPA, **b**, *in-situ* particle perovskite, **c**, *in-situ* core/shell perovskite. **d,** Energy level diagram of the pristine 3D, *in-situ* particle, *in-situ* core/shell perovskites obtained from parameters derived from UPS spectra.

Fig. 3 | Luminescent property and defect passivation with BPA treatment. a, Steady-state PL spectra and **b,** PL lifetime curves of Glass/BufHIL/Perovskite thin films that used 3D, *in-situ* particle, and *in-situ* core/shell structure. For comparison, PL intensity of 3D and *in-situ* particle perovskites in **a** were 10 times magnified. **c-e,** Two-dimensional (2D) map of temperature-dependent PL spectra of 3D, *in-situ* particle, *in-situ* core/shell perovskite film respectively (normalized to peak value).

Fig. 4 | EL characteristics of PeLEDs with BPA treatment. a, schematics of energy diagram of PeLEDs. **b**, luminance vs voltage, **c**, EQE vs luminance, and **d**, EQE histogram of PeLEDs. **e,** Summary of the reported green PeLEDs characteristics based on maximum EQE and luminance. **f,** Photograph of operating large-area device. (pixel size: 120 mm^2) **g,** Luminance vs time of PeLEDs based on *in-situ* core/shell perovskites at various initial brightness. **h**, half-lifetime vs brightness from accelerated lifetime test of *in-situ* core/shell structure PeLEDs. **i**, Summary of the reported PeLEDs characteristics based on maximum EQE and estimated or measured half-lifetime at 100 cd m^{-2}.

Methods

Materials. Formamidinium bromide (FABr, > 99.99 %), methylammonium bromide (MABr, > 99.99 %), and guanidinium bromide (GABr, > 99.99 %) were purchased from Dyesol. Cesium bromide (CsBr), BPA, tetrafluoroethylene-perfluoro3,6-dioxa-4-methyl-7-octene-sulfonic acid copolymer (PFI), chlorobenzene (CB), tetrahydrofuran (THF), and molybdenum oxide (MoO_3) were purchased from Sigma-Aldrich. Lead bromide ($PbBr_2$ >98.0 % (T)) was purchased from TCI Co., Ltd. 2,2',2"-(1,3,5-benzinetriyl)-tris(1-phenyl-1-H-benzimidazole) (TPBi) was purchased from OSM. 9,10-di(naphthalene-2-yl)anthracen-2-yl-(4,1-phenylene)(1-phenyl-1H-benzo[d]imidazole) (ZADN) was purchased from Shinwon Chemtrade Co., Ltd. Lithium fluoride (LiF) was supplied from Foosung Co., Ltd. Unless otherwise stated, all materials are used without purification.

Preparation of MHP solution. The mixed-cation precursor, $((FA_{0.7}MA_{0.1}GA_{0.2})_{0.87}Cs_{0.13}PbBr_3)$ was prepared by dissolving stoichiometric ratio of each of FABr, MABr, GABr, CsBr and $PbBr_2$ (molar ratio (FABr + MABr + GABr + CsBr) : $PbBr_2$ = 1.15 : 1) in DMSO at a concentration of 1.2 M[7,35]. In case of precursor solution for the *in-situ* particle perovskite, 10 mol. % of BPA relative to $PbBr_2$ were added. The solution was stirred overnight in N_2-filled glove box at room temperature before use.

Fabrication of PeLEDs. Pre-patterned FTO(350 nm, 12-14 Ω/sq, 25 mm × 25 mm, Nippon Sheet Glass Co., Ltd.) glasses were sonicated in acetone and 2-propanol for 15 min each sequentially, then boiled in 2-propanol for 30 min. The surface of FTO substrates undergoes ultraviolet-ozone (UVO) treatment to achieve hydrophilic surface. We used a previously-described method to prepare a HIL (BufHIL) that has a gradient work function (WF), by inducing vertical self-organization of PEDOT:PSS (CLEVIOS P VP AI4083) and tetrafluoroethylene-perfluoro3,6-dioxa-4-methyl-7-octene-sulfonic acid copolymer (PFI) to have surface-enriched PFI buffer layer; the solution with 1:1 weight ratio of PEDOT:PSS to PFI was spin-coated to form 75-nm thickness, then annealed at 150 ℃ for 30 min[1]. After baking, the substrates were transferred into a N_2-filled glove box for deposition of MHP layer. MHP films with thickness of 270 nm were deposited by spin-coating the precursor solution at 6000 rpm with additive-assisted nanocrystal pinning (NCP) process:[3] during the

15

420   second spin step, TPBi-dissolved CB solution was dropped onto the spinning perovskite film.

421   For synthesis of *in-situ* core/shell perovskite film, BPA dissolved in THF solution was loaded

422   on top of the perovskite, followed by reaction time of 30s and direct spin-drying afterward.

423   Samples were then moved to the vacuum chamber ($<10^{-7}$ Torr) to sequentially deposit ZADN

424   (45 nm), LiF (1.2 nm), and Al (100 nm). The active area of 4.9 mm^2 was defined by shadow

425   masking during deposition of cathode. Finally, the fabricated PeLEDs were encapsulated in a

426   glovebox under a controlled N_2 atmosphere (O_2 <10.0 ppm, H_2O <1.0 ppm) by using a glass

427   lid and UV-curable epoxy resin with 15 min of UV (365 nm) treatment.

428

429   **Perovskite film characterizations.** Images of the surfaces were obtained using a field-

430   emission scanning electron microscope (SEM) (SUPRA 55VP). XPS and UPS spectra were

431   measured by using a hotoelectron spectrometer (AXIS-Ultra DLD, Kratos Inc.). A

432   monochromatic Al-Kα line (1486.6 eV) was used for XPS, and He I radiation (21.2 eV) was

433   used for UPS. Steady-state photoluminescence (PL) spectra and ultraviolet/visible (UV-Vis)

434   absorption spectra were measured by using a JASCO FP8500 spectrofluorometer and

435   Lambda-465 UV-Vis spectrophotometer. For transient PL decay measurement, a system

436   composed of a streak camera (c10627, Hamamatsu Corp.) and a nitrogen pulse laser (337 nm,

437   20 Hz, Usho Inc.) was used. PLQY was measured with a PMT and monochromator (Acton

438   Research Corporation) using a 325 nm He:Cd CW laser (Kimmon Koha) at the excitation

439   power of 62.5 mW cm^{-2}. Direct and indirect emission from the perovskite film was measured

440   to determine the accurate PLQY values. For the temperature-dependent PL measurement, the

441   sample was mounted in a cryostat (Advanced Research Systems, Inc.) under vacuum and the

442   emission spectrum was analyzed using a 405 nm laser diode (PicoQuant) at excitation power

443   of 34 μW cm^{-2}. For single-carrier device analysis, MoO_3 (30 nm) and Au (50 nm) were

444   thermally deposited sequentially onto FTO / BufHIL / perovskite and encapsulated in N_2

445   atmosphere to obtain the current-voltage curve using a Keithley 236 source measurement

446   unit.

447

448   **Transmission electron microscopy characterizations.**

449   Perovskite thin films were deposited on a 5-nm-thick silicon nitride membrane using the same

450   spin-coating conditions as for the actual device. The membrane, with a size of

451     $100\,\mu m \times 1{,}500\,\mu m$, is supported on a 100-µm-thick silicon frame. The silicon nitride

452   membrane grid was loaded on a sample holder for TEM characterization without further

453   processing of TEM sample preparation. Double Cs-corrected (S)TEM systems (Themis Z,

454   Thermo Fischer Scientific) equipped with EELS (Quantum ER965, Gatan) and EDX (Super-

455   X EDS system) were used for atomic-scale structure imaging and chemical analysis of the

456   samples at an accelerating voltage of 200 kV. Due to the electron beam damage of core/shell

457   perovskite nanocrystals by high-energy electron illumination in TEM, we acquired high-

458   resolution TEM images, high-resolution STEM-HAADF images, and EELS and EDS data at

459   the low dose-rates. Core-loss EELS using a 2 Å nominal probe size and 1.8-2.0 eV energy

460   resolution were obtained with exposures of 12 sec (integrated by 60 scans with each taking for

461   0.2 sec). EELS entrance aperture of 5 mm, and an energy dispersion of 0.5 eV/ch and 1.0 eV/ch

462   were used for high-loss EELS (>1500 eV).

463

464   **Characterization on efficiency of PeLEDs.**

465   Electroluminescence efficiencies of the fabricated PeLEDs were measured using a Keithley

466   236 source measurement unit and a Minolta CS-2000 spectroradiometer. External quantum

467   efficiency of PeLEDs was calculated by measuring full angular electroluminescence

468   distribution[27]. The accuracy of the analysis was cross-checked by conducting an independent

469   analysis at the University of Cambridge with same devices, from which we confirmed

470   consistent results (**Supplementary Fig. 7**).

471

472   **Lifetime analysis of PeLEDs.** Operational lifetime of PeLEDs was measured under constant

473   current condition by simultaneously tracking brightness and applied voltage using a M760

474   Lifetime Analyzer (McScience Inc.) with a control computer under air-conditioned

475   environment below 18°C.

476

477   **Optical Simulation.** Outcoupling efficiency, perovskite reabsorption A_{act}, and parasitic

478   absorption A_{para} were obtained from the calculated Poynting vectors at each interface of glass

479   ($n = 1.5$, incoherent)/ FTO ($n = 1.9$, 350 nm)/ BufHIL ($n = 1.5$, 75 nm)/ perovskite / ZADN

480   ($n = 2$, 45 nm)/ LiF ($n = 1.4$, 1.2 nm)/ Al (n from literature[36]), by using a recently-proposed

481   method[30,31] (n: refractive index). The imaginary part of the refractive index spectrum of

482   perovskite was obtained from the measured absorbance, while the real part was assumed to

483   be constant ($n_{perov} = 2.3$). The internal radiation spectrum was obtained by the reverse

484   calculation from the measured external radiation spectrum. The maximum EQE values with

485   photon recycling effect were obtained at each perovskite thickness, by integrating the results

486   for dipoles with various wavelengths, orientations (vertical and horizontal), polarizations (s

487   and p), and positions (20 positions uniformly distributed over the perovskite layer). The

488   relationship between external and internal PLQE was calculated in the same way, for the

489   structure of glass/ perovskite.

490

491   35.   Cho, H. *et al.* High-Efficiency Polycrystalline Perovskite Light-Emitting Diodes Based
492   on Mixed Cations. *ACS Nano* **12**, 2883–2892 (2018).

493   36.   Palik, E. D. & Ghosh, G. *Handbook of optical constants of solids*. (Academic Press,
494   1998).

495

496 **Data availability**

497   The data that support the findings of this study are available from the corresponding authors

498   upon reasonable request.

499

Extended Data Fig. 1 | Morphology of *in-situ* particle perovskite thin films. SEM images of perovskite thin films made of 1.2M precursor solution with **a**, 0 % (3D), **b**, 2.5 %, **c**, 5 %, **d**, 10 % (*in-situ* particle) molar ratio of BPA molecule relative to PbBr$_2$. **e,** HAADF-STEM image and EDS elemental maps of P (green), Br (yellow), and Pb (red), respectively. **f,** HAADF-STEM image and EDS elemental maps of a single perovskite grain showing the uniform dispersion of P (green), Br (yellow), and Pb (red) on the grain.

Extended Data Fig. 2 | Morphological characterization during *in-situ* core/shell nanoparticle synthesis process. a, SEM image of a perovskite thin film (after 1s of reaction time with BPA-THF solution) showing small grains cracked out from large 3D grain. **b**, STEM image of 50 nm-size perovskite crystal during in-situ core/shell synthesis process. Yellow arrows indicate the defective perovskite surfaces that can be bound with BPA. **c**, HR-TEM image of another perovskite crystal showing ultra-small nanocrystals segregated during in-situ core/shell synthesis process. Insets: Magnified HR-TEM images of ultra-small nanocrystals taken from the white-boxed regions labelled C1 and C2. **d-e,** High-resolution HAADF-STEM images of single perovskite nanograins with decreasing grain size. Magnified HAADF-STEM images of the grain surfaces (D1, D2, E1, E2, F1, F2, G1, G2) demonstrate that the BPA shell coverages on the grain surfaces gradually increase and the defective surface regions decrease as the grain size decreases.

Extended Data Fig. 3 | Characterization of perovskite/BPA core/shell interface. a, High-resolution HAADF-STEM image of single perovskite grain formed during *in-situ* core/shell synthesis process. **b, c,** Atomic-scale HAADF-STEM (**b**) and ABF-STEM (**c**) images of the boxed area denoted in **a**. **d**,**e**, Magnified HAADF-STEM (**d**) and ABF-STEM (**e**) images of the boxed area shown in **b** and **c** to indicate the positions of EELS acquisition. **f**, EEL spectra acquired at the atomic positions labelled A, B, and C in **d**, **e**. **g**, EEL spectrum in the energy-loss range of the N-K and O-K edges acquired at the position labelled C. The O-K peak indicates the presence of BPA shells, but N-K peak is simply a background signal from the silicon nitride TEM window grid.

Extended Data Fig. 4 | SEM image of low-concentration (0.6 M) perovskite thin films with different reaction time between BPA solution and perovskite thin film. a, 3D perovskites without reaction, **b**, 1 s, **c**, 15 s, **d**, 30 s of exposure time to BPA-THF solution before spin-drying. Colored regions indicate *in-situ* particle perovskites (red) and *in-situ* core/shell perovskites (green). **e**, Schematic illustration of the growth process of BPA macroparticle domain and perovskite crystal forming *in-situ* core/shell structure.

Extended Data Fig. 5 | HAADF-STEM analysis of in-situ core/shell perovskites. a, TEM image and **b**, **c**, magnified HAADF-STEM images of *in-situ* core/shell thin films. **d**, HAADF-STEM image of *in-situ* core/shell grains and EDS elemental maps of P (red), Pb (yellow), and Br (green), respectively. The EDS maps clearly show the uniform dispersion of P (red) over macrograins. e, HAADF-STEM image of single macrograins consists of in-situ core/shell nanoparticles. **f**, EDS spectrum acquired at the location of the red circled region in **e**.
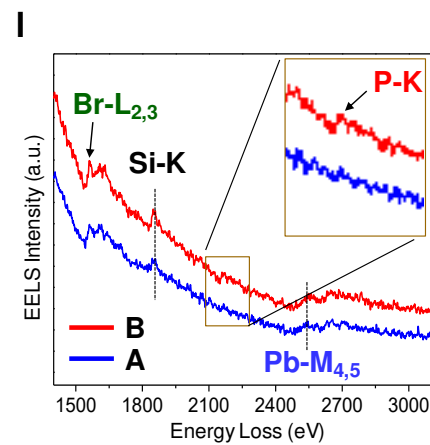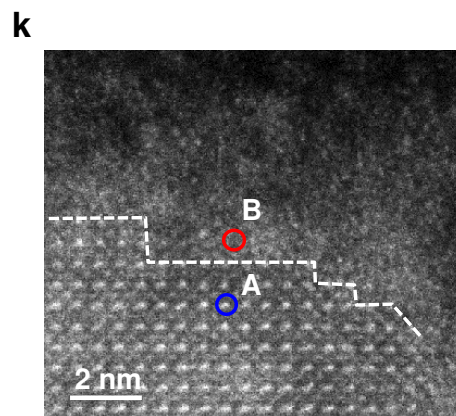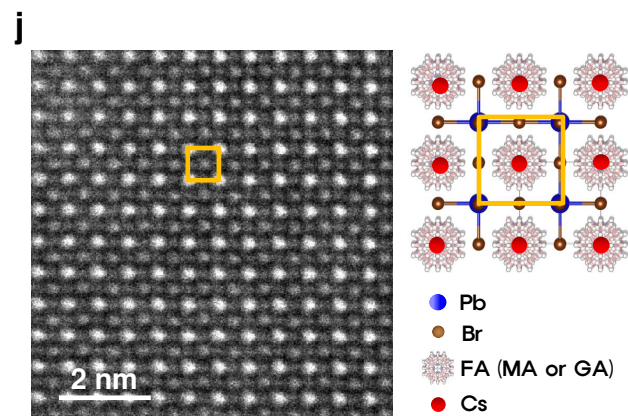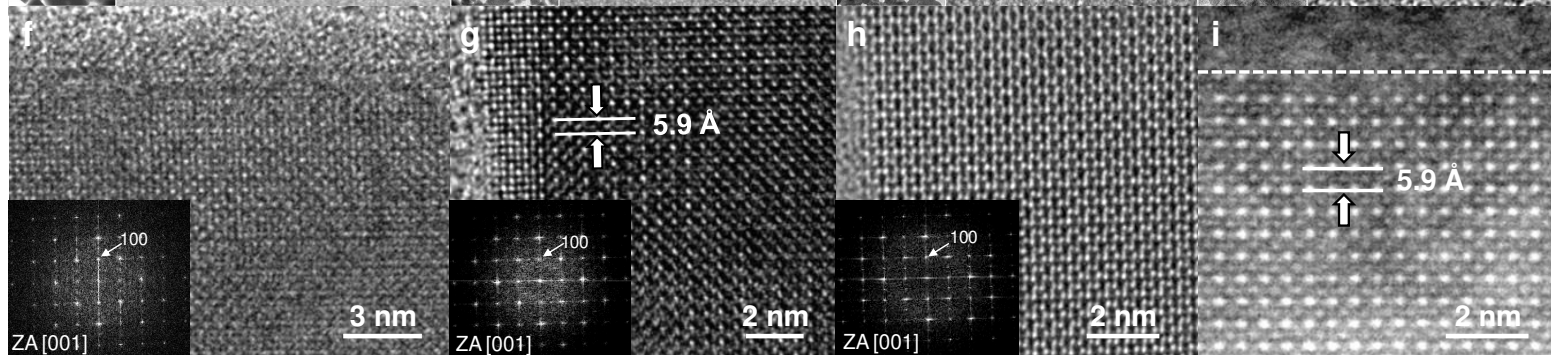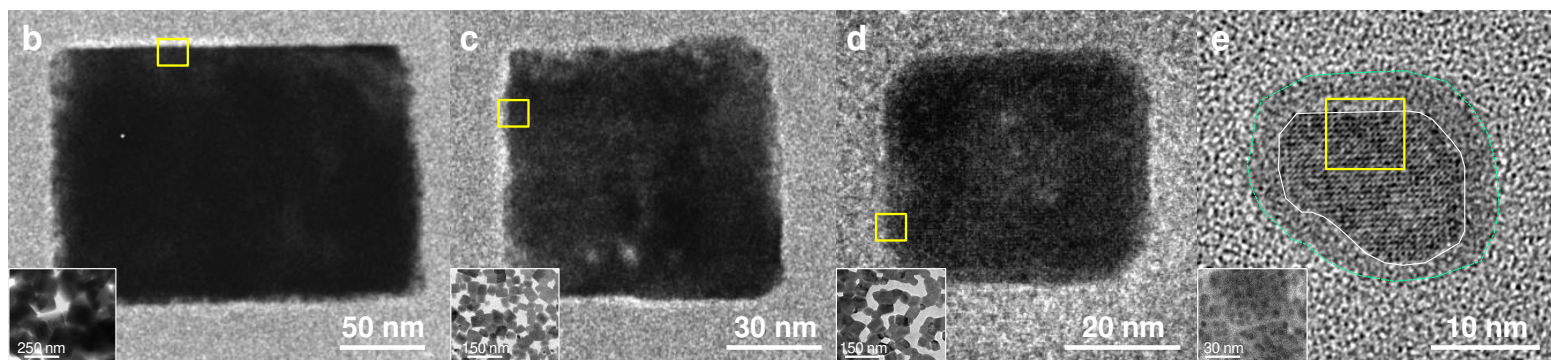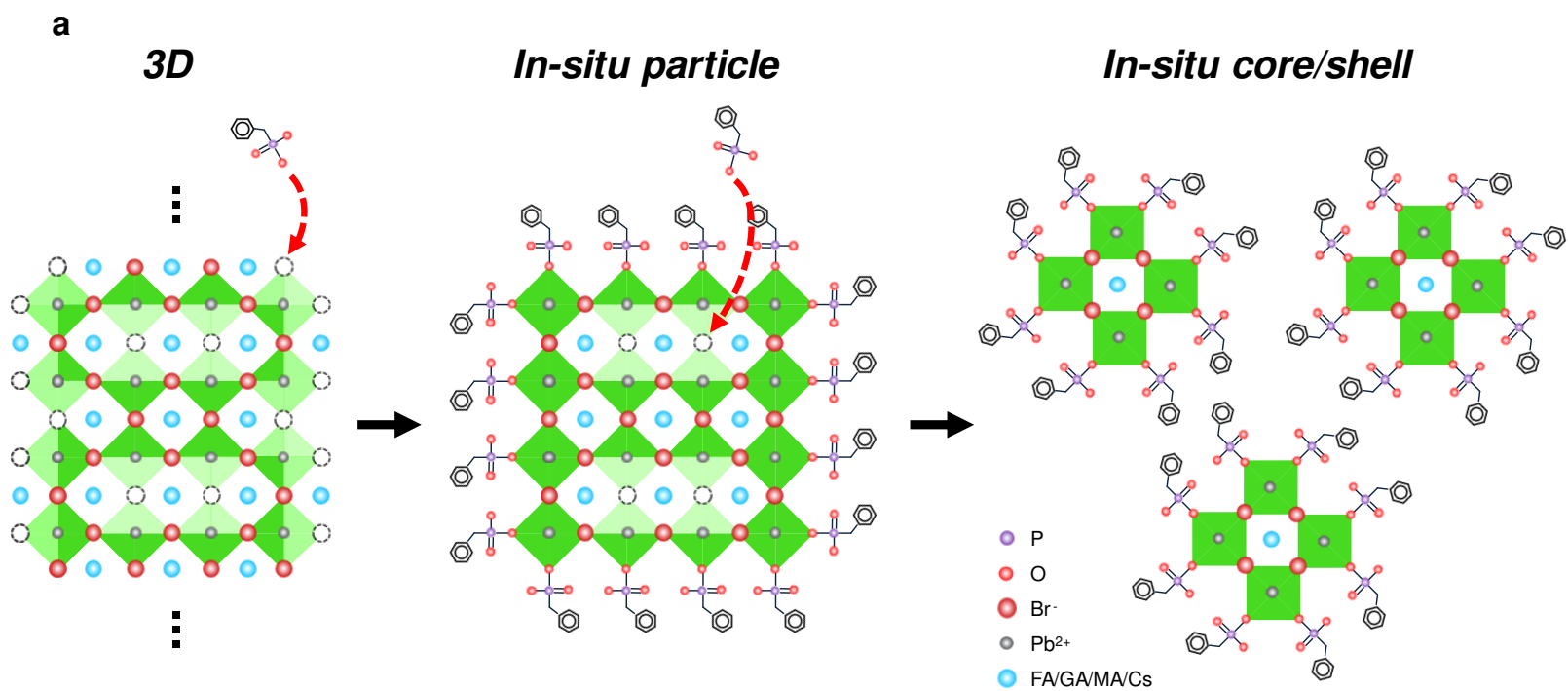
Extended Data Fig. 6 | Photoluminescence characteristics of perovskite thin films. a, PL spectra and **b**, normalized PL spectra of quartz/perovskite thin film measured in integrating sphere. **c**, External PLQE vs internal radiation efficiency (η_{rad}) (i.e. internal quantum efficiency, IQE) of perovskite film calculated considering the influence of perovskite reabsorption[30,31]. The external PLQE of *in-situ* core/shell structure was 46 %, which corresponds to IQE of 88 %. Temperature-dependent PL spectrum and corresponding integrated PL intensity with calculated activation energy of **d,g**, 3D, **e,h**, *in-situ* particle, **f,i**, *in-situ* core-shell perovskite thin films.
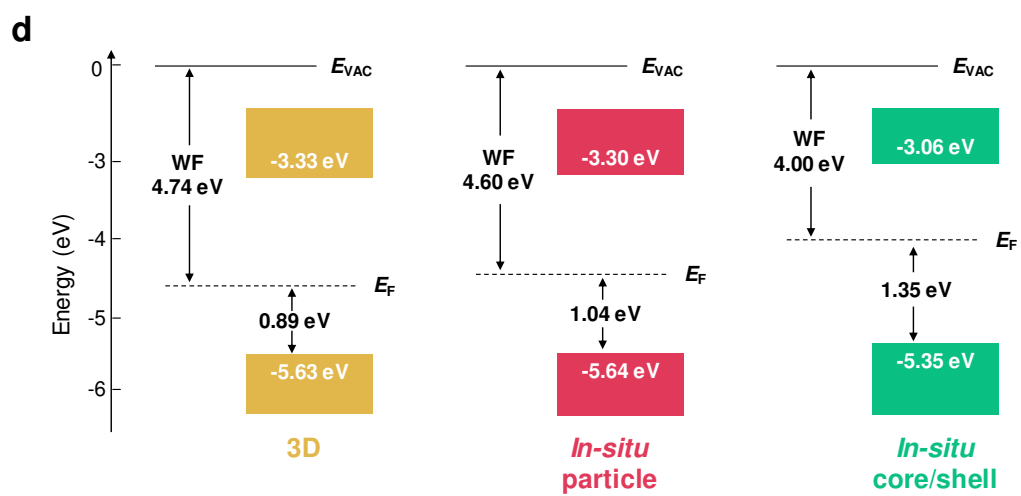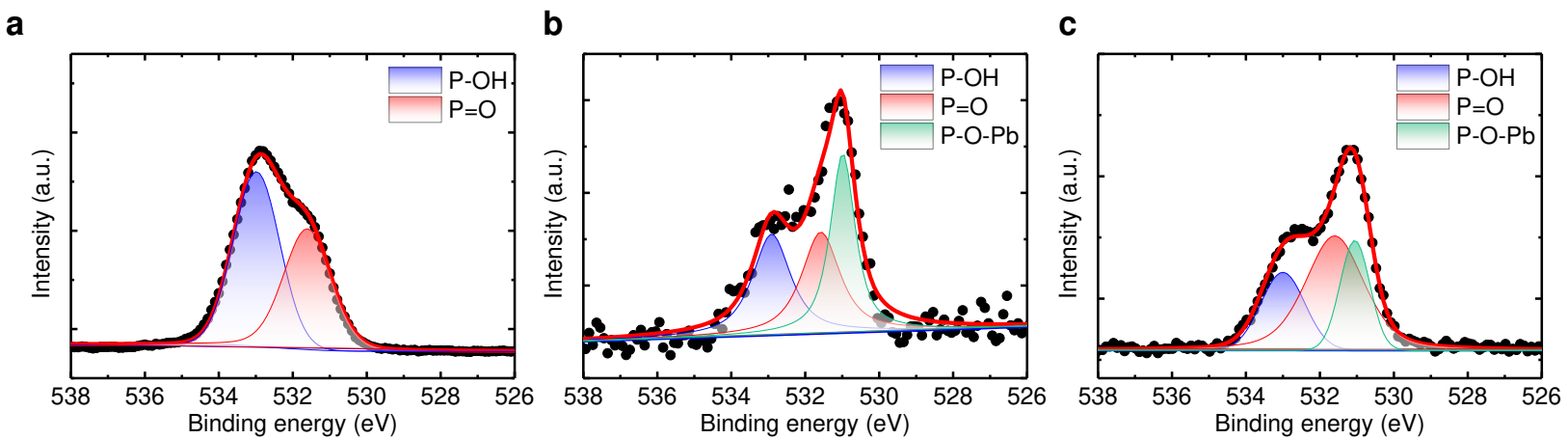
Extended Data Fig. 7 | Current-voltage-luminance characteristics of PeLEDs. a, Current density vs voltage; **b**, luminance vs current density; **c**, Normalized EL spectra; **d**, CIE coordinate of *in-situ* core/shell PeLEDs. **e**, power efficiency vs luminance; **f**, current efficiency vs luminance of PeLEDs based on 3D, *in-situ* particle, *in-situ* core/shell structure. **g**, Angle-dependent EL intensity and **h**, luminance histogram of PeLEDs based on *in-situ* core/shell structure. **i**, EQE histogram of the PeLEDs based on *in-situ* core/shell structure with different processing condition. As the temperature of the glove box increases or the A-NCP process is delayed, the grain size of the spin-coated perovskite thin film increases, which slows the penetration of the BPA solution into perovskite crystal and prevents full conversion of them into the *in-situ* core/shell structure.
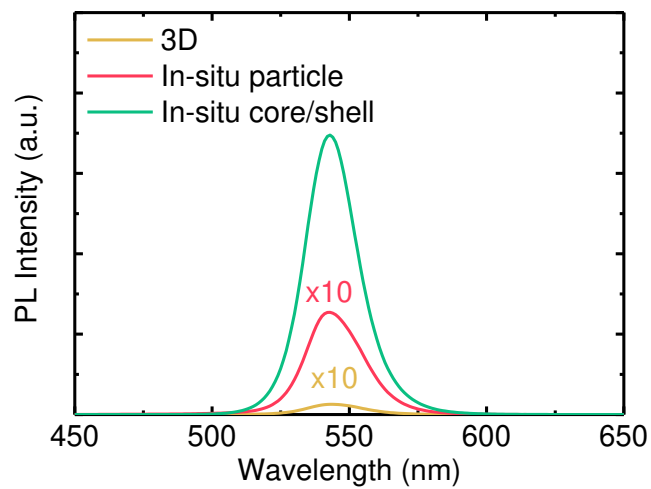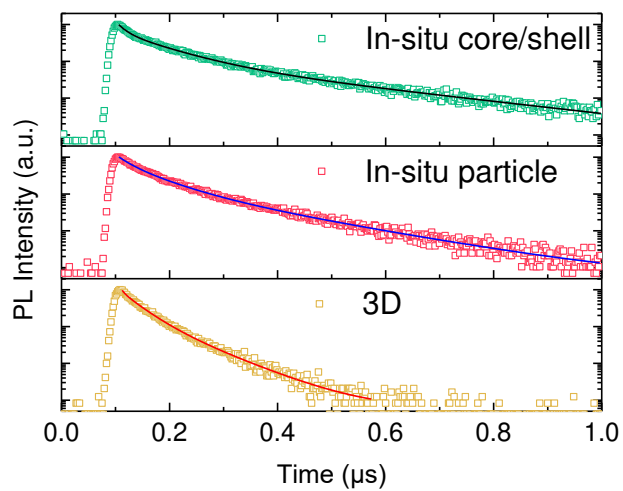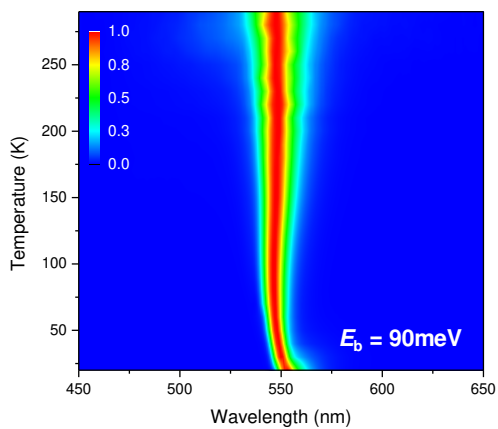
Extended Data Fig. 8 | Large-area devices. a, luminance vs voltage, **b**, EQE vs current density of large-area devices based on *in-situ* core/shell perovskites. Photographs of large-area devices (Pixel size: 120 mm^2) operating at **c**, <10 cd m^{-2}, **d**, 1,000 cd m^{-2}, **e**, 100,000 cd m^{-2}, and f, 100,000 cd m^{-2} under daylight, showing uniform emission over the pixel.

Extended Data Fig. 9 | Operational lifetime of PeLEDs. a, Luminance vs time of PeLEDs based on 3D, *in-situ* particle, and *in-situ* core/shell perovskites at initial brightness of 10,000 cd m^{-2} and **b**, corresponding driving voltage vs operation time.

Extended Data Table 1 | Summarized electrical and luminance characteristics of PeLEDs.
$V_{turn-on}$: Voltage at luminance of 1 cd m^{-2}, L_{max}: maximum luminance, EQE_{max}: maximum EQE, CE_{max}: maximum current efficiency.

a

3D *In-situ particle* *In-situ core/shell*

- P
- O
- Br⁻
- Pb²⁺
- FA/GA/MA/Cs

b 250 nm | 50 nm
c 150 nm | 30 nm
d 150 nm | 20 nm
e 30 nm | 10 nm

f ZA [001] | 3 nm
g 5.9 Å | ZA [001] | 2 nm
h ZA [001] | 2 nm
i 5.9 Å | 2 nm

j 2 nm
- Pb
- Br
- FA (MA or GA)
- Cs

k B A | 2 nm

l
Br-L₂,₃ · Si-K · P-K · Pb-M₄,₅ · B · A
EELS Intensity (a.u.) · Energy Loss (eV) · 1500 1800 2100 2400 2700 3000

a

b

c

d

a

b

c $E_b = 90\text{meV}$

d $E_b = 98\text{meV}$

e $E_b = 220\text{meV}$

a

Energy (eV)

FTO GraHIL 3D In-situ particle In-situ core/shell ZADN LiF/Al

b

Luminance (cd/m²) vs Voltage (V)

- 3D
- In-situ particle
- In-situ core/shell

c

EQE (%) vs Luminance (cd m⁻²)

d

Count vs EQE (%)

- 3D
- In-situ particle
- In-situ core-shell

e

EQE (%) vs Luminance (cd/m²)

This work

- Polycrystal
- Quasi-2D
- NP

f

g

Luminance (cd m²) vs Time (h)

- 20,000nit
- 10,000nit
- 6,000nit
- 2,500nit
- 1,500nit
- 1,000nit
- 100nit

h

Half-lifetime (hr) vs Initial brightness (cd m⁻²)

n=1.68

i

EQE (%) vs Lifetime (hour)

This work

- Blue
- Green
- Red
- IR